

Development of new technology for coal gasification purification and research on the formation mechanism of pollutants

Shu Zheng (✉ shuzheng@ncepu.edu.cn)

North China Electric Power University

Yixiang Shi

Tsinghua University

Zhiqi Wang

Chinese Academy of Sciences

Gang Liu

China Huaneng Group Clean Energy Research Institute

Huaichun Zhou

Northeast Electric Power University

Research

Keywords: IGFC, coal gasification, H₂S-CO₂ removal, syngas mercury removal

Posted Date: June 22nd, 2020

DOI: <https://doi.org/10.21203/rs.3.rs-36229/v1>

License:   This work is licensed under a Creative Commons Attribution 4.0 International License.

[Read Full License](#)

Development of new technology for coal gasification purification and research on the formation mechanism of pollutants

Shu Zheng^{1,*}, Yixiang Shi², Zhiqi Wang³, Gang Liu⁴, Huaichun Zhou⁵

¹National Engineering Laboratory for Biomass Power Generation Equipment, North China Electric Power University, Beijing 102206, China

²Key Laboratory for Thermal Science and Power Engineering of Ministry of Education, Department of Energy and Power Engineering, Tsinghua University, Beijing 100084, China

³Qingdao Institute of Bioenergy and Bioprocess Technology, Chinese Academy of Sciences, Qingdao 266101, China

⁴State Key Laboratory of Clean Coal-based Energy, China Huaneng Group Clean Energy Research Institute Co., Ltd., Changping District, Beijing 102209, China

⁵School of Energy and Power Engineering, Northeast Electric Power University, Jilin 132012, China

*Corresponding author. E-mail: shuzheng@ncepu.edu.cn

Abstract: Coal-fired power generation is the main source of CO₂ emission in China. To solve the problem of efficiency decline and cost increase caused by CO₂ capture of coal-fired power generation, Prof. Peng (Peng and Han 2009) proposed an integrated gasification fuel cell (IGFC) power generation technology. The interaction mechanism of coal gasification purification, fuel cell and other components need to be further study in the IGFC. To develop new technology for coal gasification and purification, we studied gasification reaction characteristics of ultrafine coal particles, ash melting characteristics and effects on coal gasification reaction, the formation mechanism of pollutants and developed an elevated temperature pressure swing adsorption rig for H₂S and CO₂ simultaneous removal. The results show that the Miura-Maki model appropriate to perform gasification kinetics of Shenhua bituminous coal and the predicted DTG curves fit the experimental data well. The designed 8-6-1 cycle procedure can effectively remove CO₂ and H₂S simultaneously, and the removal rate is over 99.9%. In addition, the transition metal oxides used as mercury removal adsorbents in coal gasification syngas has great potential. The technique presented in this paper can improve the gasification efficiency and reduce the formation of pollutants for IGFC.

Keywords: IGFC; coal gasification; H₂S-CO₂ removal; syngas mercury removal

1. Introduction

Entrained flow coal gasification technology, whose carbon conversion rate and cold gas efficiency can be as high as 98% and 80% respectively, represent the direction of coal gasification. Liquid slagging and dry feeding coal gasification technology has many

advantages such as low oxygen consume, high carbon conversion, high cold gas efficiency, and large capacity for single furnace, which will be the mainstream of advanced coal gasification (Liu and Tian 2012). Pulverized coal with Low ash melting point has often been used in dry feeding entrained flow gasification. Gasifying temperature should be higher than ash melting

point to ensure the liquid ash removal (Krishnamoorthy and Pisupati 2015). The successful development of large energy efficient ultrafine pulverized coal preparation system establishes the foundation for the utilization of ultrafine pulverized coal. Microscale effect of ultrafine pulverized coal can increase the gasification rate and conversion efficiency (Liu et al. 2014; Luo et al. 2019). This paper intends to perform the research on gasification characteristics of ultrafine pulverized coal under CO₂ atmosphere, and describe the basic kinetic characteristics of ultrafine pulverized coal, to provide theoretical guidance for achieving higher effective gas yield, carbon conversion rate and cold gas efficiency.

At present, the general coal gasification reaction model does not consider the thermal deactivation effect of coal at high temperature, high pressure and high conversion rate. The most commonly used kinetic models for coal gasification reaction include homogeneous model, core-shrinking reaction model and random hole model. Homogeneous model can only describe the process in which the rate of gasification reaction decreases monotonously with the rate of carbon conversion. However, it is not applicable to the gasification process with extreme gasification reaction rate. Although the stochastic pore model can describe the extreme gasification reaction rate, it is not suitable to describe the catalytic gasification process of coal and the extreme value of gasification reaction rate occurs in the case of high conversion rate. So far, no model can accurately describe the process of gasification reaction rate changing with reaction time and conversion rate. Therefore, the establishment of a generalized and quantitative kinetic model to describe coal gasification reaction will be the focus of coal gasification reaction dynamics research.

The distributed activation energy model (DAEM) (Pitt 1962) and carbon burnout kinetic model (CBK) (Cloke et al. 2003; Hurt et al.

1998a; Hurt et al. 1998b) have been proven very successful for describing the kinetics of coal pyrolysis and combustion. The DAEM was originally proposed by Pitt (Pitt 1962) and was later adapted by Anthony and Howard (Anthony and Howard 1976). It describes a complex reaction as a number of parallel first-order reactions, each occurring with its own rate coefficient. Usually, it is further assumed that all reactions share the same frequency factor and that measuring the relationship between the distributed activation energy and the burnout ratio requires at least three different heating rates. The CBK model was proposed by Hurt (Hurt et al. 1998b). It accurately describes the kinetics of heterogeneous char oxidation reactions. One of the main limitations of this type of research is that burning and burnout temperatures are always lower than the ash flow temperature (AFT). The kinetic characteristics of coal high-temperature combustion require further investigation. In this study, the kinetic parameters of the char combustion including the activation energy (E) and pre-exponential factor (A) were obtained from thermogravimetric analyzer (TGA) data. A model that predicted the char combustion rate was then established using the kinetic parameters of char combustion and was validated with experimental data.

In the field of syngas purification, there are several industrialized methods which could separately remove H₂S and CO₂, such as Selexol, methyldiethanolamine (MDEA), rectisol and pressure swing adsorption (PSA) (Chaubey et al. 2013; Dincer and Acar 2015; Wiheeb et al. 2013; Yu et al. 2012). These techniques are widely used in coal chemical industry, providing a basis for the development of H₂S-CO₂ simultaneous removal methods. Selexol, rectisol and MDEA belong to wet method, in which impurities are absorbed by solvents at -50~60 K. The solvent in MDEA is chemical absorbent while the others are physical absorbent. The devices of wet methods are complicated and costly. Impurity

removal and absorbents regeneration are conducted in different units. The maintenance and operating costs are not economical either.

Therefore, some substitutes of conventional purification methods are proposed and studied. Using dry methods, RTI international (Denton and L 2014; Gupta and Raghbir 2010) separated H₂S and CO₂ from syngas at elevated temperature and normal temperature, respectively, more than 99.9% of the H₂S and 90% of the CO₂ being captured. Compared with Selexol and rectisol, the initial investment of this method decreased by 50% and the operating cost was also lower. The energy consumption of adsorbent/absorbent regeneration is only 72% of that in Selexol.

Moreover, if H₂S and CO₂ could be simultaneously removed in one step, the device would be further simplified. However, the corresponding techniques are still under development. Improvement of adsorbent performance, technique process design and adsorption bed structure optimization are all necessary at this stage.

With the rapid development of human society, energy and environmental problems are becoming more and more serious. However, China's rich in coal, poor in oil and gas determines that coal will be the main fossil energy to maintain the rapid development of the whole society in a long period of development. Accordingly, sulfur, nitrogen, chlorine and other pollutants generated in the process of coal utilization have been widely concerned (Xu and Wei 1999); The trace and volatile metal elements (such as Hg, Pb, As, Se, etc.) has also been paid more attention. Mercury is the most volatile heavy metal pollutant in coal. Although its concentration in coal is relatively low, the output and consumption of coal are very large, and mercury is mainly discharged in the form of gas, so the mercury discharged in the process of coal utilization accounts for a large proportion of the mercury released by human activities.

With more and more attention paid to the mercury pollution in the air, the mercury emission in the process of coal utilization has become an urgent environmental problem to be solved. There are three forms of mercury released from coal utilization: Hg^p, Hg²⁺ and Hg⁰. Hg^p can be removed by particulate control equipment, Hg²⁺ can be removed by wet scrubbing or SO₂ control equipment, while elemental mercury is not easy to dissolve, so it is difficult to remove it by ordinary dust removal equipment (Pavlish et al. 2003). In recent years, the research work of mercury removal mainly focuses on the removal of mercury from coal-fired flue gas. The main methods are: ① Adsorption method: adsorption of mercury in flue gas with activated carbon, fly ash, mineral adsorbents, etc. (Granite et al. 2000; Liu 2015); ② Catalytic adsorption method: metal oxides (such as TiO₂, CeO₂, ZnO, MoO₃, CuO, MnO₂, etc.) (Li et al. 2011; Liu 2016; Wen et al. 2011) or precious metals (Ag, Pd, Pt, etc.) (Liu et al. 2008) are loaded on Al₂O₃ or molecular sieve and other carriers to remove mercury. The two methods show a certain ability of mercury removal in different temperature ranges, but the components of flue gas (SO₂, SO₃, NO, NO_x, HCl, etc.) have a great influence on the mechanism of mercury removal. The gas produced by coal gasification is composed of reducing atmosphere (usually containing trace O₂), and the content of elemental mercury that is difficult to remove is higher than that of coal-fired flue gas (Pavlish et al. 2003; Reed et al. 2001). Therefore, the removal of mercury from coal gas atmosphere has gradually become a research hotspot at home and abroad, and the Research of mercury removal is the key of efficient mercury removal technology.

2. Methods and Experiments

2.1 CO₂ gasification of ultrafine coal particles

Bituminous coal obtained from Shenhua

mine was used in this work. Screening equipment was used to separate materials with five particle sizes, and their average particle sizes were determined by Malvern Mastersizer 3000. Thermogravimetric analysis was conducted with a TG (Setsys Evolution, SETARAM, France). Each sample was heated under CO₂ atmosphere from ambient temperature to 1300 °C with four different heating rates (5, 10, 20, and 40 °C/min). The integral iso-conversional model proposed by Miura-Maki (Miura and Maki 1998) was used to perform the kinetic analysis.

$$\ln\left(\frac{\beta}{T^2}\right) = \ln\left(\frac{k_0 R}{E}\right) + 0.6075 - \frac{E}{RT} \quad (1)$$

Where β is the heating rate; k_0 is the pre-exponential factor; E is the activation energy; R is the universal gas constant; T is the absolute temperature (K).

2.2 Model building of coal gasification

2.2.1 Kinetic model of char combustion

At low combustion reaction temperatures, the chemical reaction rate is not very fast and the oxygen supply rate is much faster than the chemical reaction oxygen consumption rate. Therefore, the combustion process consisted of slow heating and the combustion reaction zone can be considered a dynamic area, where the chemical kinetic factors control the reaction rate (Sun and Chen 1991). The reaction rate can be expressed with the Arrhenius law and the assumptions are as follows (Zhang et al. 2000):

(a) The sample particles are spherical, and the particle diameter and density are constant during the combustion process, the impact of the ash layer on the combustion is not considered.

(b) The combustion reactions only occur on the particles' surfaces and the reaction rate is calculated based on the particles' outside surface area.

(c) The oxygen pressure is distributed evenly throughout the sample layer.

(d) The total surface reaction product is

CO₂.

The combustion rate function can be expressed as follows (Hecker et al. 2003; Sima-Ella et al. 2005):

$$\alpha = \frac{m_0 - m}{m_0 - m_\infty} \quad (2)$$

$$-\frac{d\alpha}{dt} = K(\alpha)\alpha \quad (3)$$

The reaction rate function $K(\alpha)$ is usually assumed to be the Arrhenius equation (Pilling and Seakins 1995):

$$K(\alpha) = A(\alpha) \exp(-E(\alpha) / (RT)) \quad (4)$$

where α is the burnout ratio, which is the mass fraction of the burned combustible matter with the total combustible matter in the coal; m_0 is the initial mass weight of the sample; m is the sample's mass weight at time t and m_∞ is the final sample weight; $K(\alpha)$ is the combustion reaction rate as a function of α ; $A(\alpha)$ is the pre-exponential factor function; $E(\alpha)$ is the activation energy function; T is the combustion temperature; R is the gas coefficient.

The curves of char combustion at two temperatures T_1 and T_2 can be obtained from TGA experiments including $TG_1(\alpha)$, $TG_2(\alpha)$, $DTG_1(\alpha)$, and $DTG_2(\alpha)$. The $E(\alpha)$ and $A(\alpha)$ from T_1 to T_2 can be calculated as:

$$E_{T_1-T_2}(\alpha) = -\frac{R \ln \frac{DTG_1(\alpha)}{DTG_2(\alpha)}}{\left(\frac{1}{T_1} - \frac{1}{T_2}\right)} \quad (5)$$

$$A_{T_1-T_2}(\alpha) = \frac{DTG_2(\alpha)}{\exp(-E_{T_1-T_2}(\alpha) / (RT_2))} \quad (6)$$

From Eqs. (5) and (6), the predicted combustion reaction rate function $DTG'(\alpha)$ at a combustion temperature of T_3 ($T_3 \in [T_1, T_2]$) follows:

$$DTG'(\alpha) = A_{T_1-T_2}(\alpha) \exp(-E_{T_1-T_2}(\alpha) / RT_3) \quad (7)$$

To validate the predicted model's veracity, the predicted results are compared with

experimental data and an error analysis is conducted.

2.2.2 Coal Properties and Experimental Method

Hulunbeier lignite coal was utilized in the present work. The average diameter of the coal

samples was 76 μm and all samples were less than 200 μm . The coal properties, ash components, and fusion characteristic temperatures are presented in **Table 1**.

Table 1 Coal properties (as received basis, wt.%) and ash components analysis

Item	Value	Item	Value
Coal proximate analysis		Ash compositions	
(%, w/w ar)		(wt %)	
Fixed carbon	44.86	SiO ₂	55.63
Volatile matter	35.44	Al ₂ O ₃	11.51
Ash	11.05	Fe ₂ O ₃	14.22
Moisture	8.65	CaO	11.24
Ultimate analysis		MgO	2.14
(%, w/w ar)		TiO ₂	0.76
Carbon	59.46	SO ₃	3.02
Hydrogen	3.35	P ₂ O ₅	0.06
Oxygen	16.44	K ₂ O	0.48
Nitrogen	0.80	Na ₂ O	0.94
Sulfur	0.25	Fusion characteristic temperature	
Lower heating value	25.6	(°C)	
(MJ/kg)		DT ^a	1090
		ST ^b	1100
		HT ^c	1110
		FT ^d	1160

^a Deformation Temperature. ^b Softening Temperature. ^c Hemispherical Temperature. ^d Flow Temperature.

A TGA from Beijing Henven Scientific Instrument Factory was used. The minimum sensitivity was 0.1 μg and the data was collected every second in a temperature range of 25 °C to 1450 °C.

All coal samples were measured at 20 mg, dewatered at 100 °C for 30 min, and heated at a fixed heating rate of 80 °C/min starting at 100 °C and rising to the temperature T_H with N₂ atmosphere (200 mL/min); the samples were then held at T_H for 30 min for complete volatile devolatilization. Air (100 mL/min) was then injected into the TGA after 30 min and the temperature was kept constant until the mass

weights of the samples remained constant. The temperature T_H in each case was divided into 25 levels in the range of 500~1450 °C, and using intervals of 50 °C in the range of 500~1200 °C and 25 °C in the range of 1200~1450 °C.

2.3 H₂S-CO₂ removal

The authors had proposed elevated temperature pressure swing adsorption (ETPSA) process operating at 150~400 °C for H₂S-CO₂ simultaneous removal. It is similar to PSA but the working temperature is higher. As a dry method, the device of ETPSA is less complex

than that in wet methods. Furthermore, compared with regular PSA, ETPSA is more energy efficiency due to a higher product gas recovery rate and less sensible heat loss (Gazzani et al. 2013).

A small scale (6 Nm³/h) ETPSA unit has been developed in the ammonia plant of Quanji Energy Co., Ltd., Shanxi province, China. On-site CO₂-H₂S simultaneous removal is

realized on this device. Syngas coming from water gas shift (WGS) unit flowed to this unit with a flow rate of 1~10 Nm³/h. The WGS is approximately 50 m away from ETPSA, hence the temperature decreased from 216°C to around 180°C during the transport. A part of steam condensed and separated by a gas-liquid separator. The compositions of final feed gas are listed in **Table 2**.

Table 2 Details of the feed gas

Temperature	Pressure	Composition
180°C	2-3MPa	54% H ₂ , 36% CO ₂ , 5% H ₂ O, 0.4% CO, 700 ppm H ₂ S, 1% N ₂ , 3% CH ₄ , Trace Ar

There were four adsorption beds and four buffer tanks (same sized column packed with similar sized SiO₂ particles) in this rig. The tanks are used for pressure equalization. The height of adsorption beds are 1.8 m and the inner diameter is 79 mm. The adsorbent was 207C activated carbon (Calgon Carbon Co., Ltd) which had undergone some special surface treatment(Li et al. 2019). The hydrophobicity of the adsorbent was much more better than the pristine activated carbon. The outlook of this rig is given by **Fig. 1**.



Fig. 1 The outlook photo of ETPSA device

Step	1	2	3	4	5	6	7	8	9	10	11	12	13	14	15	16	17	18	19	20	21	22	23	24
Bed1	AD	AD	AD	AD	AD	RH	PEA	PE1	PEB	PEC	PE2	PED	BD	PG	V	PEB	PE2	PEC	PEB	PE1	PEA	PP	PP	PP
Bed2	PEB	PE1	PEA	PP	PP	PP	AD	AD	AD	AD	AD	RH	PEA	PE1	PEB	PEC	PE2	PED	BD	PG	V	PEB	PE2	PEC
Bed3	BD	PG	V	PEB	PE2	PEC	PEB	PE1	PEA	PP	PP	PP	AD	AD	AD	AD	AD	RH	PEA	PE1	PEB	PEC	PE2	PED
Bed4	PEA	PE1	PEB	PEC	PE2	PED	BD	PG	V	PEB	PE2	PEC	PEB	PE1	PEA	PP	PP	PP	AD	AD	AD	AD	AD	RH
Tank1	PEA		PEA			PEA		PEA				PEA	PEA					PEA		PEA				
Tank2	PEB		PEB			PEB		PEB				PEB	PEB					PEB		PEB				
Tank3			PEC		PEC				PEC	PEC					PEC	PEC						PEC	PEC	
Tank4			PED		PED				PED	PED					PED	PED						PED	PED	
Cycle 544s	50	30	14	14	14	14	50	30	14	14	14	14	50	30	14	14	14	14	50	30	14	14	14	14
Cycle 456s	43	19	13	13	13	13	43	19	13	13	13	13	43	19	13	13	13	13	43	19	13	13	13	13
Cycle 360s	34	18	11	11	11	5	34	18	11	11	11	5	34	18	11	11	11	5	34	18	11	11	11	5
Cycle 468s	40	25	14	15	15	7	40	25	14	15	15	7	40	25	14	15	15	7	40	25	14	15	15	7

Fig. 2 8-6-1 ETPSA cycle procedures. AD: adsorption; RH: high pressure steam rinse; PE: pressure equalization with columns (1, 2) or tanks (A, B, C, D); BD: counter-current blow down; PG: N₂ purge; V: vacuum desorption; PP: pressurization with product gas.

According to elevating the working temperature, the reversibility of H₂S adsorption

was improved (Hao et al. 2019). Adsorbed H₂S could be detached from the adsorbent and

collected during vacuum desorption or purge step. Although the sulfur capacity of activated carbon was lower than metal oxides, the breakthrough times of H_2S was still much longer than CO_2 . Hence as long as CO_2 did not penetrate the adsorption bed, the H_2S could be removed thoroughly.

Herein, an 8-6-1 (eight adsorption beds/tanks, six pressure equalization, one adsorption in each cycle) ETPSA cycles were designed. The schedules are shown in **Fig. 2**, where the step sequence and the corresponding duration lengths are listed. The time length of each cycle here is 468 s (the last line in the chart). Because N_2 is a material of ammonia synthesis, N_2 purging was adopted in this study.

2.4 Syngas mercury removal

2.4.1 Preparation of Adsorbents

The precursor $Mn(NO_3)_2 \cdot 4H_2O$ of 10 g manganese oxide was dissolved in deionized water, and the volume was fixed in a 100 ml volumetric bottle to prepare 100 ml $Mn(NO_3)_2$ solution with a mass fraction of 10 wt.%. 10g activated alumina and 10 ml manganese nitrate aqueous solution were measured. Then the activated alumina was added to manganese nitrate aqueous solution, stirred manually for 30

min, and then subjected to ultrasonic shock for 20 min. The activated alumina impregnated with manganese nitrate solution was heated on the electric furnace of 200 W and placed in the oven of 100 °C for 1 h until the water evaporated. After drying, alumina loaded with manganese oxide precursor was placed in a tubular furnace at a constant temperature of 400 °C, and then removed after calcining for 3 h in an air atmosphere. It was cooled to room temperature in a drying dish. The obtained Mn_2O_3/Al_2O_3 mercury removal adsorbent was stored in silica gel.

Co_2O_3/Al_2O_3 and Fe_2O_3/Al_2O_3 adsorbents were prepared by the same method with $Co(NO_3)_2$ and $Fe(NO_3)_2$ as precursors, respectively.

2.4.2 The Device and Method of Adsorbents Evaluation

The experiment was carried out on the fixed bed reactor system, as shown in **Fig. 3**. It mainly includes 6 parts: simulated syngas control system, mercury vapor generation system, water vapor generation system, tubular reactor system, tail gas treatment system and mercury analysis system. The MAX-L cold atomic absorption mercury analyzer produced by Labtech company was used in the experiment to test the mercury concentration.

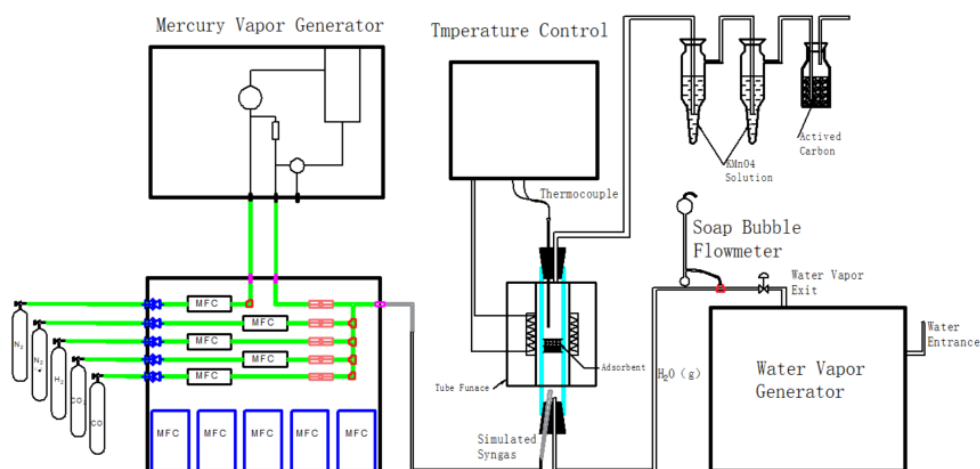


Fig. 3 Schematic diagram of simulated syngas mercury removal system

The mercury removal activity of the adsorbent was evaluated in a fixed bed reactor under 200 °C simulated gas (N₂-CO-H₂-H₂S-H₂O-Hg) atmosphere, and the experimental apparatus was shown in **Fig. 4**. Simulated gas was selected in the experiment: Hg steam concentration was 60 μg/m³, stable concentration was provided by mercury permeation tube through the dynamic gas calibration instrument, the permeation temperature was set at 60 °C, the carrier gas was N₂, and the flow rate was 200 mL/min. The simulated gas was provided by standard gas distribution cylinder, H₂S concentration of 200

ppm, H₂ volume fraction of 30%, CO volume fraction of 60%, CO₂ volume fraction of 5% and H₂O vapor volume fraction of 5%. The total gas flow rate was 1 L/min (nitrogen was the equilibrium gas), the adsorbent dose was 0.5 g, and the bed temperature was set as 200 °C.

The mercury removal efficiency (η) of adsorbent was used as the evaluation index, the calculation formula was as follows:

$$\eta = \frac{H_{gin} - H_{gout}}{H_{gin}} \quad (8)$$

where H_{gin} and H_{gout} represent the inlet and outlet Hg⁰ concentrations (ng/L) respectively.

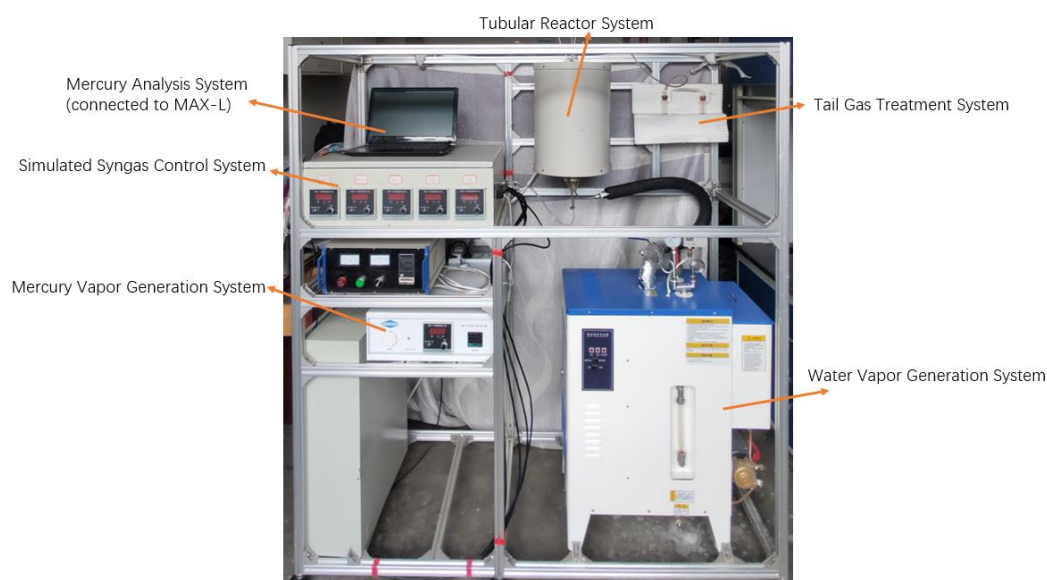


Fig. 4 Test bench of syngas mercury removal system

3. Results and discussions

3.1 CO₂ gasification of ultrafine pulverized coal particles

It can be seen from the particle size distribution curves (as shown in **Fig. 5a**) and microscopic appearance (as shown in **Fig. 5b**) that the average particle sizes for sample 1#, 2# and 3# were smaller than sample 4# and 5#. Further, the surface for 4# and 5# was smooth, while the surface for 1#, 2# and 3# was rather rough. The rough surface would promote the gasification process and enhance the reaction activity. The five gasification conversion

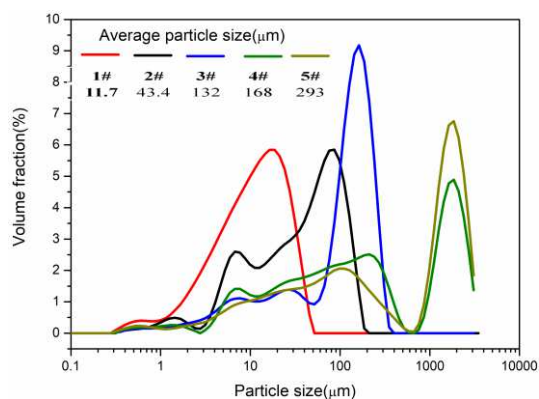
factor (α) curves for samples with different particle sizes (as shown in **Fig. 5c**) almost overlapped when the temperature was lower than 850 °C. However, when the temperature was higher than 850 °C, there were significant differences for coal samples with different particle sizes. As for the effect of particle size on the gasification conversion factor, it can be found that the smaller the particle size, the larger the value of conversion factor. According to the plot of $\ln(\beta/T^2)$ vs $1/T$ at a particular conversion factor (α) (as shown in **Fig. 5d**), a linear equation with the slope of $-E/R$ and intercept of $\ln(k_0R/E)+0.6075$ can be fitted to give the values of activation energy,

pre-exponential factor, and correlation coefficient (R^2). The calculated values of correlation coefficient for all five samples are all higher than 0.97, showing that the Miura-Maki model apply to Shenhua bituminous coal for gasification kinetic analysis.

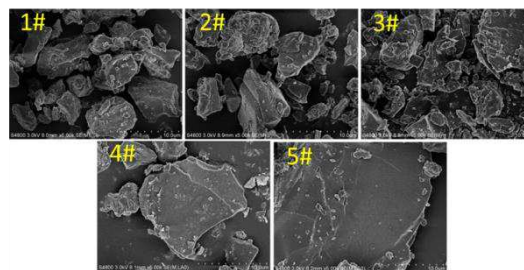
3.2 Predicted DTG model

Fig. 6 depicts the $T(t)$, $1-\alpha(t)$, $DTG(t)$, and $DTG(\alpha)$ profiles for the Hulunbeier lignite coal. As shown in **Fig. 6** (b) and (c), the weight loss ratio $1-\alpha$ and the reaction rate $DTG(t)$ exhibit a regular distribution as the combustion temperature increases. The peaks in the $DTG(\alpha)$ profiles shown in **Fig. 6** (d) can be observed when the burnout ratio α is around 0.1, which was also observed by Bhatia et al. (Bhatia and Perlmutter 1980) The authors proposed a random pore model (RPM), which stated that the reaction rate responded to the change in pore structure and that a positive relationship existed between changes in the reaction rate and pore superficial area. The changes in the pore superficial area were the result of the competition between the pore extension and the pore overlap. The pore extension benefited from the increase in pore superficial area while the result for the pore overlap was the opposite. At the beginning of char combustion, the pore extension dominated and the reaction rate increased rapidly with the increase in the pore superficial area. After the peak of the reaction rate occurred at α_{max} , the pore overlap began to dominate the reaction and the reaction rate decreased with the reduction in the pore superficial area. The peak of the reaction rate predicted by the RPM occurred at $0 < \alpha_{max} < 0.393$, which matched the observations shown in **Fig. 6** (d).

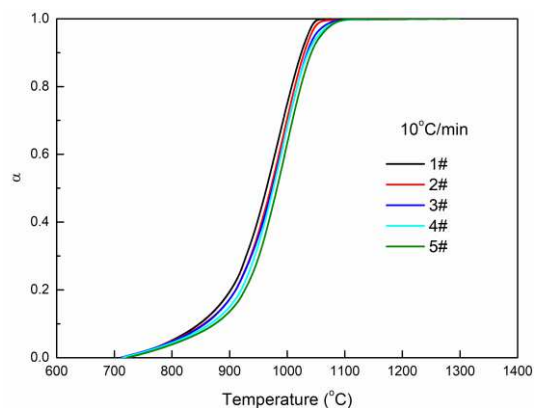
The $E(\alpha)$ and $A(\alpha)$ are obtained by Eqs. (5) and (6) and are shown in **Fig. 7**. The result shows that both the $E(\alpha)$ and $\log A(\alpha)$ exhibited a U-shaped with a gentle fluctuation in the range of $0.2 < \alpha < 0.9$. As the burnout ratio increased from 0 to 0.3, the char began to burn and the combustion rate increased significantly. This resulted in the decrease in E and $\log A$. As the combustion continued, the flammable matter burned first and heated the flame retardant matter. The combustion rate, E , and $\log A$ were relatively stable in the range of $0.2 < \alpha < 0.9$. As the



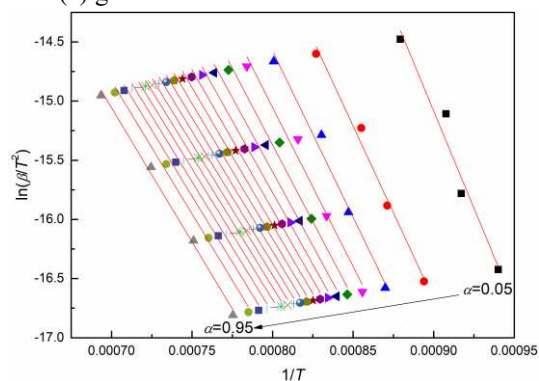
(a) particle size distribution curves



(b) the micro surface morphology

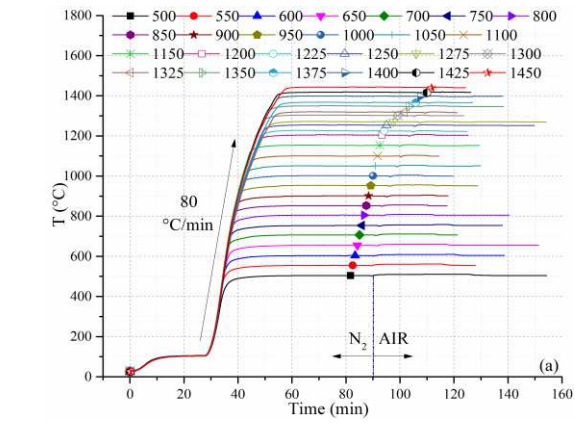


(c) gasification conversion factor curves

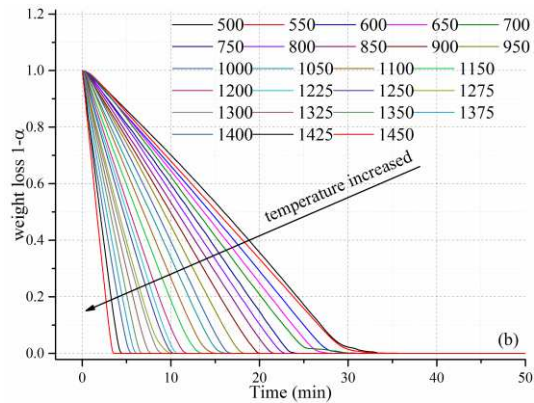


(d) the plots of $\ln(\beta/T^2)$ vs $1/T$

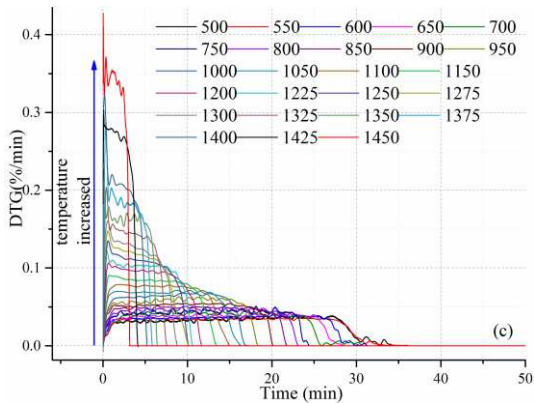
Fig. 5 Experimental results of five coal samples with different particle sizes: (a) particle size distribution curves; (b) the micro surface morphology; (c) gasification conversion factor curves; (d) the plots of $\ln(\beta/T^2)$ vs $1/T$ at a particular conversion factor



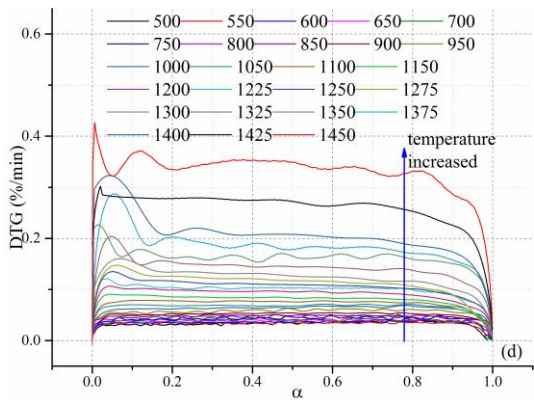
(a) $T(t)$



(b) $1-\alpha(t)$

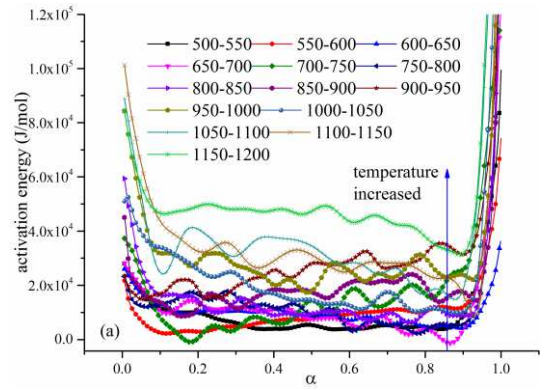


(c) $DTG(t)$

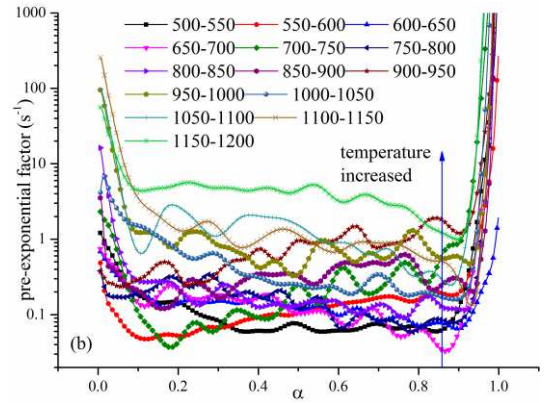


(d) $DTG(\alpha)$

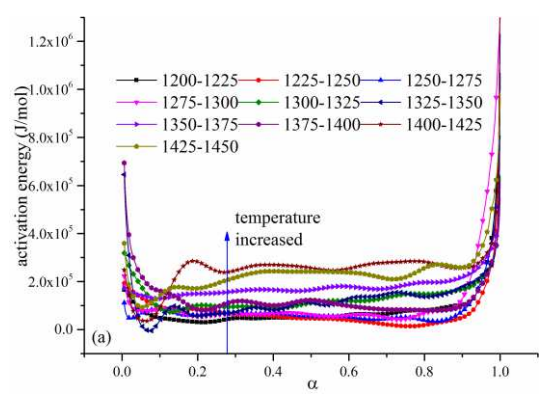
Fig. 6 The (a) $T(t)$, (b) $1-\alpha(t)$, (c) $DTG(t)$, and (d) $DTG(\alpha)$ profiles for the Hulunbeier lignite coal.



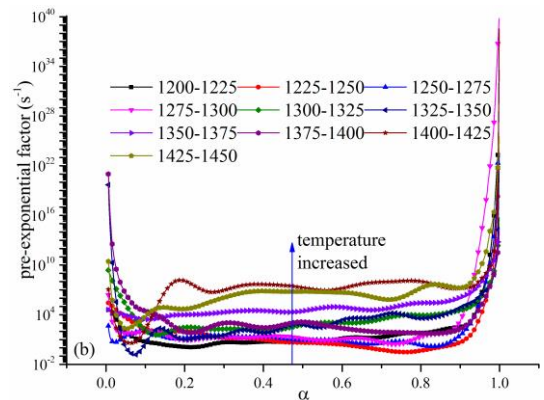
(a) activation energy $E(\alpha)$



(b) pre-exponential factor $A(\alpha)$



(a) activation energy $E(\alpha)$



(b) pre-exponential factor $A(\alpha)$

Fig. 7 The results for (a) activation energy $E(\alpha)$ and (b) pre-exponential factor $A(\alpha)$.

combustion temperature increased from 500 °C to 1200 °C, the E and logA curves progressively decreased in the range of $0.2 < \alpha < 0.9$ and increased in the range of 1200 °C to 1450 °C. At the end of the combustion $0.9 < \alpha < 1$, the E and logA curves increased exponentially for all temperatures.

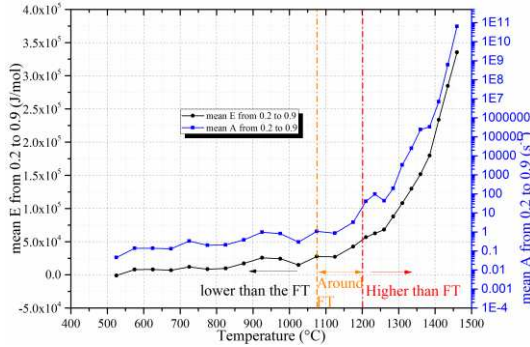
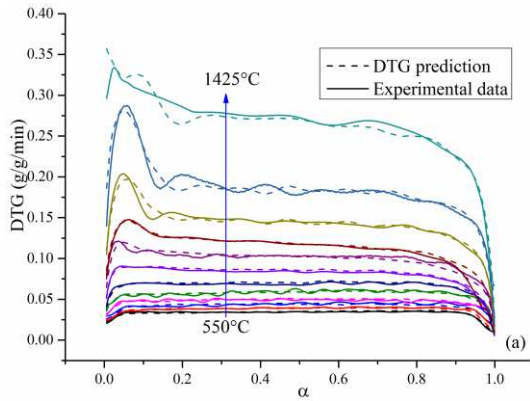
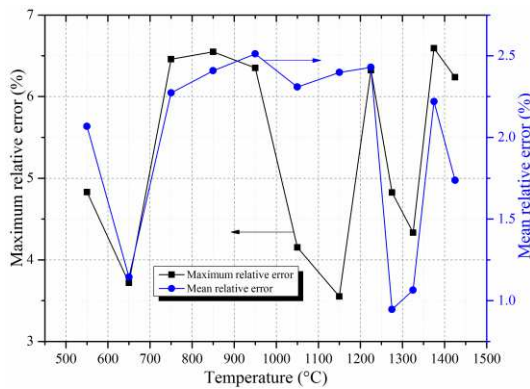


Fig. 8 The mean E and A values in the range of $0.2 < \alpha < 0.9$.



(a) predicted results and experimental results



(b) error analysis in the range of $0.2 < \alpha < 0.9$.

Fig. 9 Comparison of (a) predicted results and experimental results and (b) error analysis in the range of $0.2 < \alpha < 0.9$

The E and logA curves were stable in the range of $0.2 < \alpha < 0.9$ and the mean E and logA in this range

are shown in **Fig. 8**. At a combustion temperature lower than the AFT (1160 °C), the E and logA values fluctuated within the same order of magnitude. However, when the combustion temperature exceeded the AFT, the E and logA values increased exponentially. It is noteworthy that the mean E and A values in the range of $0.2 < \alpha < 0.9$ varied with different temperatures, especially when the combustion temperature exceeded the AFT.

The values of T_1 and T_2 were identified as close as possible to avoid the effect of the AFT on the results of E and A. Using Eqs. (5), (6), and (7), the $DTG'(\alpha)$ at a combustion temperature of T_3 ($T_3 = (T_1 + T_2)/2$) was obtained. The comparison of the predicted results and the experimental results is shown in **Fig. 9(a)**. **Fig. 9(b)** shows the error analysis in the range of $0.2 < \alpha < 0.9$. The predicted DTG curves fit the experimental data well. The maximum and mean relative errors were less than 6.5% and 2.5%, respectively. This indicated that the predicted DTG model proposed in this study was validated to predict the char combustion in the TGA; the model performed especially well for high-temperature ($T > 1200$ °C) char combustion.

3.3 H₂S-CO₂ removal

The composition of the product gas is listed in **Table 3**. The steam was removed by cooling before the evaluation. It is seen that the concentration of CO₂ was lower than 500 ppm, meaning 99.9% of the CO₂ was captured by the adsorbent. The concentration of H₂S was lower than the detection accuracy of chromatographic (0.1 ppm). H₂S removing by activated carbon seems to be feasible. After running for several months, the H₂S did not penetrate the adsorption bed, indicating the adsorption of H₂S did be reversible. As a physical adsorbent, activated carbon could more or less adsorb all kinds of gas. Therefore, not only CO₂ and H₂S but CO and CH₄ were also partially removed during this process. Because N₂ was adopted as the purging gas, the concentration of N₂ is a bit higher than the feed gas. Small amount of inert gas is acceptable when the H₂ is used in IGCC and IGFC.

Table 3 Working condition and purification outcomes of 8-6-1 ETPSA

Temperature	Pressure	Flow rate	Product gas composition (dry)
170°C	2MPa	5.7 Nm ³ /h	1~2% N ₂ , <500 ppm CO ₂ , <0.1% CO, <0.1 ppm H ₂ S, <100 ppm CH ₄ , H ₂ as balance gas

The H₂ recovery rate during this purification process is 97%, which is much higher than regular PSA (Lopes et al. 2011; Shen et al. 2012; Wang et al. 2012). It could be attributed to the introduction of vacuum desorption and steam rinse. In order to explore the influence of rinse and vacuum desorption, we changed the cycle procedure and evaluated the corresponding product gas compositions and

recovery rates. The case shown above is the best one and is named as Case 4. The others are Case 1-3. The results are as shown in Table 4. The conditions and parameters were same to Case 4 if not mentioned. We regulated the cycle time to make the product purity close Case 4 so that the recovery rate could represent the separation efficiency. The time length of each step is also given in Fig. 2.

Table 4 Separation efficiencies of different cases with and without vacuum desorption and steam rinse

Case	Temperature	Flow rate	Cycle time	H ₂ S	CO ₂	H ₂ recovery	Procedure
1	170°C	5.2 Nm ³ /h	456 s	<0.1ppm	~0.3%	79.3%	Without V and RH
2	120°C	6.8 Nm ³ /h	544 s	<0.1ppm	~0.3%	86.4%	Without V and RH
3	170°C	5.7 Nm ³ /h	360 s	<0.1ppm	~0.3%	93.3%	Without V

After replacing V and RH with PG and AD respectively, the H₂ recovery decreased to 79.3%, which was close to some regular PSA operated at normal temperatures (Mivechian and Pakizeh 2013; Rahimpour et al. 2013). Considering the adsorption capacity of activated carbon would deteriorate with the rising temperature, we set the temperature as 120 °C and the H₂ recovery rate is thus improved in Case 2. Then we added the steam rinse, H₂ recovery increasing to over 90% immediately. It means steam rinse was a significant factor. However, although the cycle time of Case 3 is shorter, the CO₂ concentration in product gas was up to 0.3%, which was much higher than Case 4. It was mainly due to the remained impurities in adsorption bed after regeneration steps. Vacuum desorption is demonstrated to be effective on the aspect of promoting adsorbent regeneration and compensate the defect in desorption kinetic performance. The introduction of vacuum

desorption will result in extra power consumption and the cost of high pressure steam in rinse step will also lead to more energy consumption. Hence the energy efficiency of ETPSA should be further discussed in our following studies.

3.4 Syngas mercury removal

3.4.1 α -Al₂O₃ measurement

The α -Al₂O₃ was carrier in the experiments, and the parameters as shown in

Table 5. It can be seen that specific surface area of α -Al₂O₃ may reach 237 m²/g, which was very large, and α -Al₂O₃ was the ideal carrier material.

Table 5 Properties of carrier α -Al₂O₃

Simple	Size/mm	specific surface area (m ² /g)
α -Al ₂ O ₃	1.5	237

3.4.2 Mercury removal test of the carrier

Mercury removal experiments were carried out at different temperatures with α -Al₂O₃, which was not impregnated with the active component. The experimental result was shown in Fig. 10. It could be seen that the temperature at 150 °C, mercury removal efficiency was about 5%. However, mercury removal efficiency decreased with the increase of temperature, when the temperature reached 400 °C, the mercury removal efficiency was almost zero. And the reason was mainly due to the α -Al₂O₃ full of the microchannel had very large specific surface area, which possessed strong physical adsorption capacity. So the α -Al₂O₃ presented the mercury removal capacity in lower temperature. But the α -Al₂O₃ don't possess chemical adsorption capacity, the mercury removal capacity was lost when the temperature reached 400 °C.

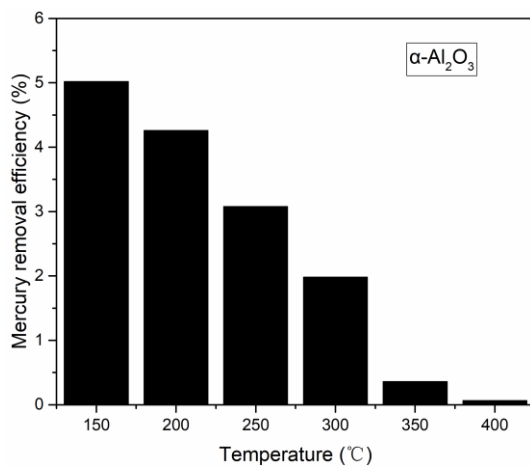


Fig. 10 Mercury removal performance of α -Al₂O₃ at different temperatures

3.4.3 Evaluation of prepared adsorbents

The prepared Mn₂O₃/Al₂O₃, Co₂O₃/Al₂O₃ and Fe₂O₃/Al₂O₃ loaded with active components were evaluated under the simulated gas condition of 200 °C respectively. The evaluation

results were shown in Fig. 11~Fig. 13.

As shown in Fig. 11~Fig. 13, the mercury removal efficiency of prepared Mn₂O₃/Al₂O₃ could reach 90.4% in the first 10 min, and then slowly decreased, and finally the mercury

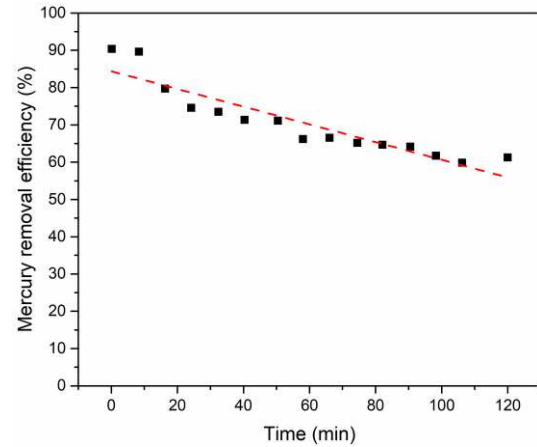


Fig. 11 The test curve of mercury removal performance of Mn₂O₃/Al₂O₃

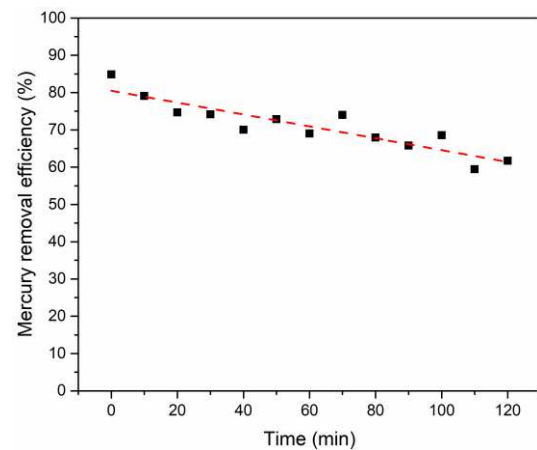


Fig. 12 The test curve of mercury removal performance of Co₂O₃/Al₂O₃

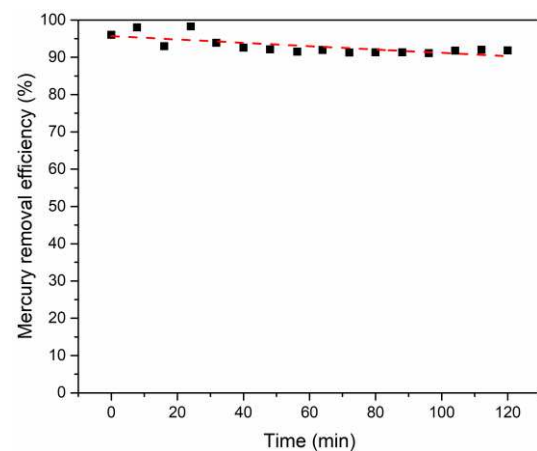
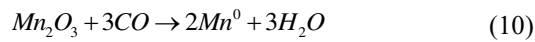
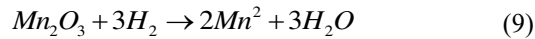


Fig. 13 The test curve of mercury removal performance of Fe₂O₃/Al₂O₃

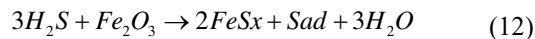
removal efficiency was stable at about 60%. The initial mercury removal efficiency of the prepared $\text{Co}_2\text{O}_3/\text{Al}_2\text{O}_3$ was 86%, and the final mercury removal efficiency was stable at about 60%. The mercury removal agent $\text{Fe}_2\text{O}_3/\text{Al}_2\text{O}_3$ had the best mercury removal performance, with the initial mercury removal efficiency reaching 95.4%. In the two-hour test, the mercury removal agent was maintained at about 90% with no attenuation.

It could be seen in Fig. 11 and 12, the mercury removal efficiency of $\text{Mn}_2\text{O}_3/\text{Al}_2\text{O}_3$ and $\text{Co}_2\text{O}_3/\text{Al}_2\text{O}_3$ both showed very big promotion compared to pure Al_2O_3 , which presented that the way of the original physical adsorption was changed, and speculated that physical adsorption and chemical adsorption synergy effected existed (Huo et al. 2017; Mao et al. 2018), the mechanism was speculated as follows (Mn_2O_3 as example):



Meanwhile, the mercury removal efficiency of $\text{Mn}_2\text{O}_3/\text{Al}_2\text{O}_3$ and $\text{Co}_2\text{O}_3/\text{Al}_2\text{O}_3$ both displayed the trend of decreasing during 2 h test, finally the mercury removal efficiency was stable at a certain value, which suggested that the reaction of Hg^0 and the active component reached reaction equilibrium.

The mercury removal mechanism of $\text{Fe}_2\text{O}_3/\text{Al}_2\text{O}_3$ was obviously different from that of $\text{Mn}_2\text{O}_3/\text{Al}_2\text{O}_3$ and $\text{Co}_2\text{O}_3/\text{Al}_2\text{O}_3$. The mechanism was speculated as follows:



It could be seen that because H_2S existed in coal gasification syngas improved the mercury removal efficiency and stability of $\text{Fe}_2\text{O}_3/\text{Al}_2\text{O}_3$ mercury removal agent, H_2S replaced the combination of transition metal oxides with Hg^0 ,

making its mercury removal efficiency reached more than 90%.

4. Conclusions

In this paper, the gasification reaction characteristics of ultrafine coal particles, the formation mechanism of pollutants, and H_2S and CO_2 simultaneous removal in the process of IGFC were studied. The following conclusions can be obtained.

(1) The surface became coarser with the decrease of the particle size of coal sample, which would promote the gasification process and improve the reaction activity. It was proved that the Miura-Maki model appropriate to perform gasification kinetics of Shenhua bituminous coal. The value of activation energy decreased with the decrease of the particle size of coal samples.

(2) A database of the kinetic characteristics functions of char combustion was established and a DTG model was established. The maximum and mean relative errors were less than 6.5% and 2.5%, respectively. The predicted DTG curves fit the experimental data well because the effect of the AFT on the E and A values was taken into account.

(3) A small scale ETPSA rig was built in an ammonia plant and on-site syngas $\text{H}_2\text{S}-\text{CO}_2$ simultaneous removal was realized. An 8-6-1 cycle procedure with steam rinse and vacuum desorption was designed and demonstrated to be efficient. The concentration of CO_2 and H_2S in product gas was lower than 500 ppm and 0.1 ppm respectively, indicating the removal rate was over 99.9%. The corresponding H_2 recovery rate was 97%. The importance of steam rinse and vacuum desorption was verified after changing the cycle procedure. However, the energy efficiency of ETPSA should be analyzed in detail in the future.

(4) Three kinds of mercury removal adsorbents were prepared, $\text{Mn}_2\text{O}_3/\text{Al}_2\text{O}_3$, $\text{Co}_2\text{O}_3/\text{Al}_2\text{O}_3$, $\text{Fe}_2\text{O}_3/\text{Al}_2\text{O}_3$, which showed

different degrees of mercury removal performance. Among them, the mercury removal efficiency of $\text{Fe}_2\text{O}_3/\text{Al}_2\text{O}_3$ was basically stable at more than 90% under the 2 h condition of 200 °C medium temperature test. The use of transition metal oxides as mercury removal adsorbents in coal gasification syngas had great potential and was the main direction of the research on mercury removal in IGFC gas purification system.

Acknowledgements:

This work was financially supported by National Key R&D Program of China (2017YFB0601900).

References

- Anthony DB, Howard JB (1976) Coal devolatilization and hydrogasification. *AIChE Journal* 22(4):625-656.
- Bhatia SK, Perlmutter D (1980) A random pore model for fluid-solid reactions: I. Isothermal, kinetic control. *AIChE Journal* 26(3):379-386.
- Chaubey R, Sahu S, James OO, Maity S (2013) A review on development of industrial processes and emerging techniques for production of hydrogen from renewable and sustainable sources. *Renewable & Sustainable Energy Reviews* 23:443-462.
- Cloke M, Wu T, Barranco R, Lester E (2003) Char characterisation and its application in a coal burnout model. *Fuel* 82(15):1989-2000.
- Denton, L D (2014) An update on RTI's warm syngas cleanup demonstration project. Paper presented at the Gasification Technologies Conference, Washington, DC.
- Dincer I, Acar C (2015) Review and evaluation of hydrogen production methods for better sustainability. *International journal of hydrogen energy* 40(34):11094-11111.
- Gazzani M, Macchi E, Manzolini G (2013) CO₂ capture in integrated gasification combined cycle with SEWGS – Part A: Thermodynamic performances. *Fuel* 105:206-219.
- Granite EJ, Pennline HW, Hargis RA (2000) Novel Sorbents for Mercury Removal from Flue Gas. *Industrial and Engineering Chemistry Research* 39(4):1020.
- Gupta, Raghubir (2010) Scaleup and Commercialization of Warm Syngas Cleanup Technology with Carbon Capture and Storage. Paper presented at the Gasification Technologies Conference, Washington, DC.
- Hao P, Liu Z, Shi Y, Li S, Cai N (2019) Characteristics of activated carbon in elevated-temperature pressure swing adsorption desulfurization. *Adsorption* 25(6):1-8.
- Hecker WC, Madsen PM, Sherman MR, Allen JW, Sawaya RJ, Fletcher TH (2003) High-pressure intrinsic oxidation kinetics of two coal chars. *Energy & fuels* 17(2):427-432.
- Huo Q, Qi D, Ye L, Han L, Chang L (2017) The Preparation of PdFe/Al₂O₃ Mercury Removal Sorbent by Chemical Co-Precipitation. *Chemical Reaction Engineering & Technology* 33(5):450-457.
- Hurt R, Sun J-K, Lunden M (1998a) A kinetic model of carbon burnout in pulverized coal combustion. *Combustion and Flame* 113(1):181-197.
- Hurt R, Sun JK, Lunden M (1998b) A Kinetic Model of Carbon Burnout in Pulverized Coal Combustion. *Combustion & Flame* 113(1):181-197.
- Krishnamoorthy V, Pisupati SV (2015) A Critical Review of Mineral Matter Related Issues during Gasification of Coal in Fixed, Fluidized, and Entrained Flow Gasifiers. *Energies* 8(9):10430-10463.
- Li H, Wu CY, Li Y, Zhang J (2011) CeO₂-TiO₂ Catalysts for Catalytic Oxidation of Elemental Mercury in Low-Rank Coal

- Combustion Flue Gas. *Environmental Science & Technology* 45(17):7394-7400.
- Li S, Hao P, Zhu X, Shi Y, Jiang H (2019) On-site demonstration of an elevated temperature hydrogen clean-up unit for fuel cell applications. *Adsorption* 25(8):1683-1693.
- Liu B, Tian J (2012) Progress in effects of coal properties on entrained-flow gasification. *Chemical Industry and Engineering Progress* 31(10):2191-2196(in chinese).
- Liu J, Jiang X, Han X, Shen J, Zhang H (2014) Chemical properties of superfine pulverized coals. Part 2. Demineralization effects on free radical characteristics. *Fuel* 115:685-696.
- Liu T (2016) Mechanism and experimental study on removal of elemental mercury by iron oxide. Dissertation, Huazhong university of science and technology
- Liu X (2015) Theoretical study of removal of γ -Al₂O₃ for hydrogen sulfide and mercury. Dissertation, Taiyuan university of technology
- Liu Y, Kelly DJA, Yand H, Lin CCH, Kuznicki SM, Xu Z (2008) Novel Regenerable Sorbent for Mercury Capture from Flue Gases of Coal-Fired Power Plant. *Environmental Science & Technology* 42(16):6205-6210.
- Lopes FVS, Grande CA, Rodrigues AE (2011) Activated carbon for hydrogen purification by pressure swing adsorption: Multicomponent breakthrough curves and PSA performance. *Chemical Engineering Science* 66(3):303-317.
- Luo L, Yao W, Liu J, Zhang H, Ma J, Jiang X (2019) The effect of the grinding process on pore structures, functional groups and release characteristic of flash pyrolysis of superfine pulverized coal. *Fuel* 235:1337-1346.
- Mao J, Zhou J, Li X, Zhou Q, Cao H (2018) Mechanism of Mercury Removal in Syngas by Co-modified Activated Coke with H₂S. *Chinese Journal of Applied Chemistry* 35(12):106-115(in chinese).
- Miura K, Maki T (1998) A Simple Method for Estimating $f(E)$ and $k_0(E)$ in the Distributed Activation Energy Model. *Energy & Fuels* 12(5):864-869.
- Mivechian A, Pakizeh M (2013) Hydrogen recovery from Tehran refinery off-gas using pressure swing adsorption, gas absorption and membrane separation technologies: Simulation and economic evaluation. *Korean Journal of Chemical Engineering* 30(4):937-948.
- Pavlish JH, Sondreal EA, Mann MD, Olson ES, Benson SA (2003) Status review of mercury control options for coal-fired power plants. *Fuel Processing Technology* 82(2):89-165.
- Peng S, Han M (2009) Development of Coal/Carbon Based Solid Oxide Fuel Cell. *Chinese Journal of Nature* 31(4):187-192(in chinese).
- Pilling MJ, Seakins PW (1995) *Reaction Kinetics*. Oxford University Press, New York
- Pitt G (1962) The kinetics of the evolution of volatile products from coal. *Fuel* 41(3):267-274.
- Rahimpour MR, Ghaemi M, Jokar SM, Dehghani O, Jafari M, S. Amiri, S. Raeissi (2013) The enhancement of hydrogen recovery in PSA unit of domestic petrochemical plant. *Chemical Engineering Journal Lausanne*
- Reed GP, Ergudenler A, Grace JR, Watkinson AP, Herod AA, Dugwell D, Kandiyoti R (2001) Control of gasifier mercury emissions in a hot gas filter: the effect of temperature. *Fuel* 80(5):623-634.
- Shen C, Liu Z, Li P, Yu J (2012) Two-Stage VPSA Process for CO₂ Capture from Flue Gas Using Activated Carbon Beads. *Industrial & Engineering Chemistry Research* 51:5011-5021.
- Sima-Ella E, Yuan G, Mays T (2005) A simple kinetic analysis to determine the intrinsic reactivity of coal chars. *Fuel*

- 84(14):1920-1925.
- Sun X, Chen J (1991) Physical and chemical basis of pulverized coal combustion. HUST Press, Wuhan
- Wang L, Liu Z, Li P, Wang J, Yu J (2012) CO₂ capture from flue gas by two successive VPSA units using 13XAPG. Adsorption 18(5-6):445-459.
- Wen X, Li C, Fan X, Gao H, Zhao Y (2011) Experimental Study of Gaseous Elemental Mercury Removal with CeO₂/γ-Al₂O₃. Energy & Fuels 25(7):2939–2944.
- Wiheeb AD, Shamsudin IK, Ahmad MA, Murat MN, Kim J, Othman MR (2013) Present technologies for hydrogen sulfide removal from gaseous mixtures. Reviews in Chemical Engineering 29(6):449-470.
- Xu S, Wei S (1999) An analysis and evaluation of the gas clean-up process equipment and technical equipment characteristics in four IGCC demonstration power plants. Clean Coal Technology 5(1):47-51(in chinese).
- Yu CH, Huang CH, Tan CS (2012) A Review of CO₂ Capture by Absorption and Adsorption. Aerosol and Air Quality Research 12(5):745-769.
- Zhang X, Nie Q, Sun S (2000) A study of thermobalance model for the burning of blended coals. Journal of Engineering for Thermal Energy and power 15(4):356-359(in chinese).

Figures

Small-scale pilot of PSA at elevated temperature at Fengxi Ammonia Plant



Figure 1

The outlook photo of ETPSA device

Step	1	2	3	4	5	6	7	8	9	10	11	12	13	14	15	16	17	18	19	20	21	22	23	24
Bed1	AD	AD	AD	AD	AD	RH	PEA	PE1	PEB	PEC	PE2	PED	BD	PG	V	PED	PE2	PEC	PEB	PE1	PEA	PP	PP	PP
Bed2	PEB	PE1	PEA	PP	PP	PP	AD	AD	AD	AD	AD	RH	PEA	PE1	PEB	PEC	PE2	PED	BD	PG	V	PED	PE2	PEC
Bed3	BD	PG	V	PED	PE2	PEC	PEB	PE1	PEA	PP	PP	PP	AD	AD	AD	AD	AD	RH	PEA	PE1	PEB	PEC	PE2	PED
Bed4	PEA	PE1	PEB	PEC	PE2	PED	BD	PG	V	PED	PE2	PEC	PEB	PE1	PEA	PP	PP	PP	AD	AD	AD	AD	AD	RH
Tank1	PEA		PEA																					
Tank2	PEB		PEB																					
Tank3				PEC		PEC																		
Tank4				PED		PED																		
Cycle 544s	50	30	14	14	14	14	50	30	14	14	14	14	50	30	14	14	14	14	50	30	14	14	14	14
Cycle 456s	43	19	13	13	13	13	43	19	13	13	13	13	43	19	13	13	13	13	43	19	13	13	13	13
Cycle 360s	34	18	11	11	11	5	34	18	11	11	11	5	34	18	11	11	11	5	34	18	11	11	11	5
Cycle 468s	40	25	14	15	15	7	40	25	14	15	15	7	40	25	14	15	15	7	40	25	14	15	15	7

Figure 2

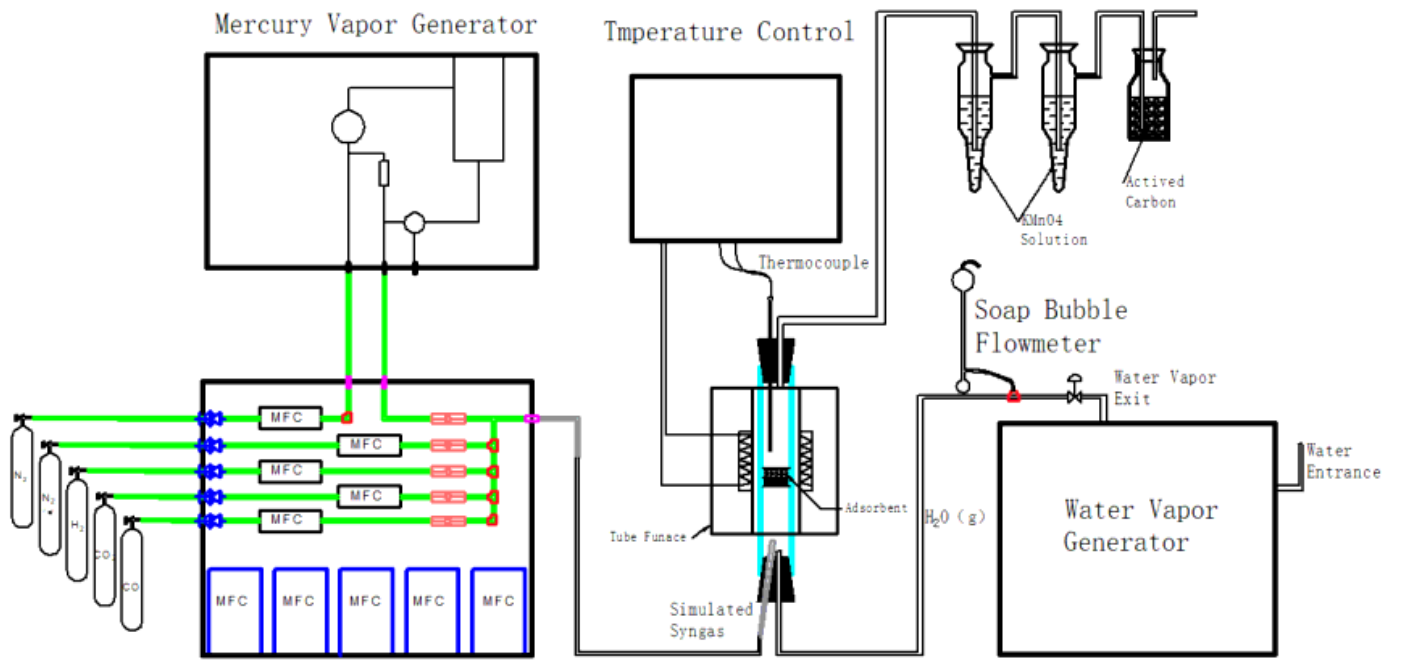


Figure 3

Schematic diagram of simulated syngas mercury removal system

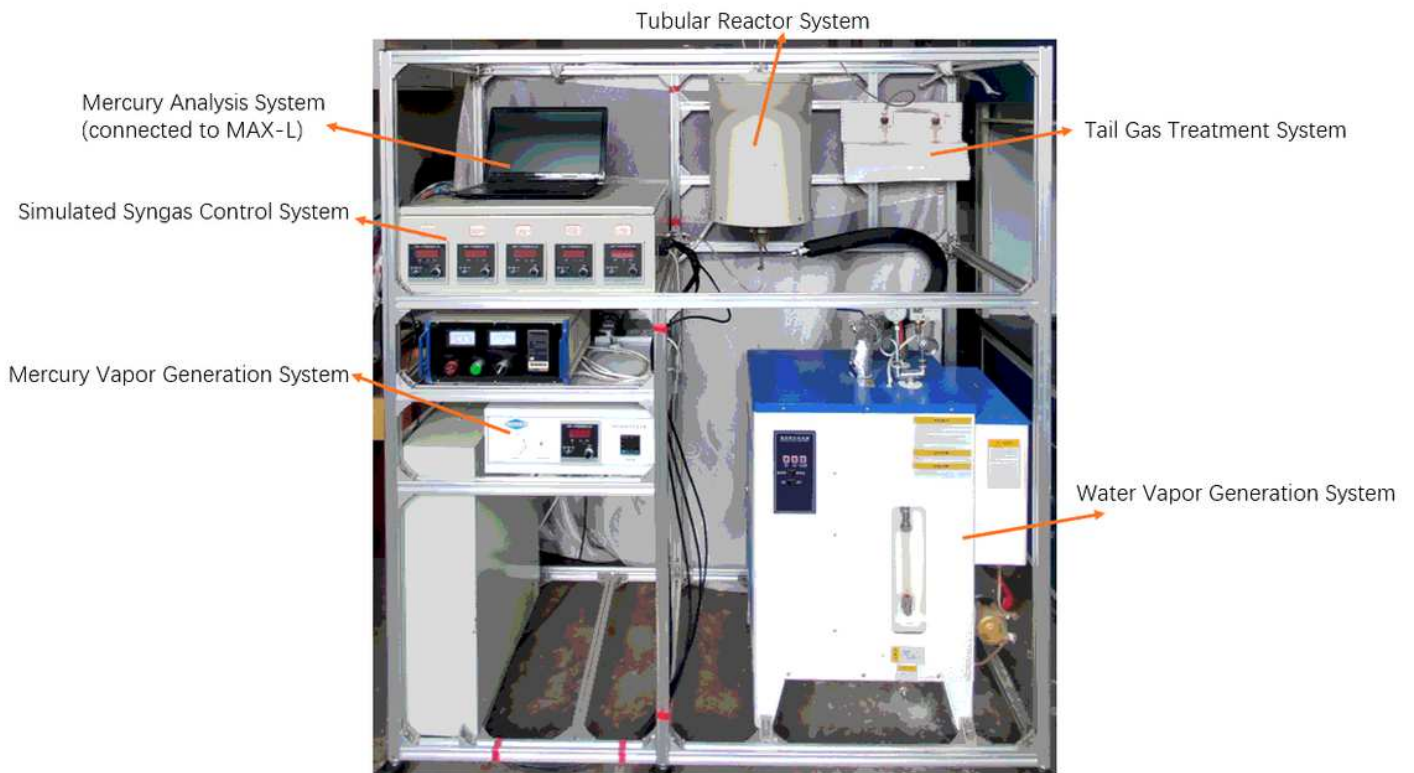
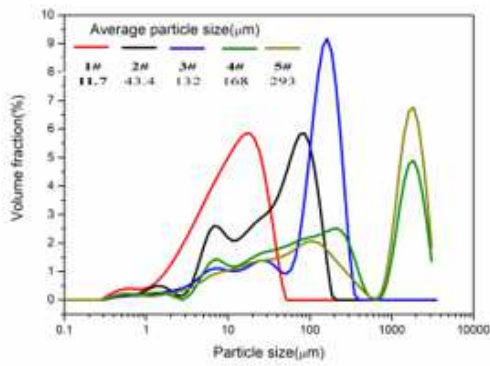
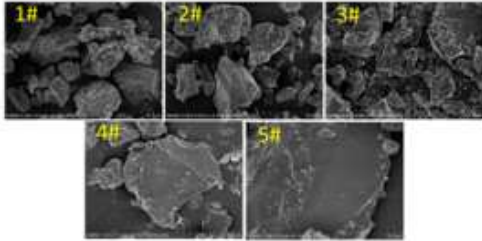


Figure 4

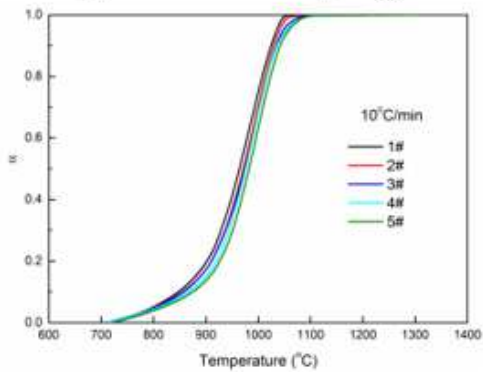
Test bench of syngas mercury removal system



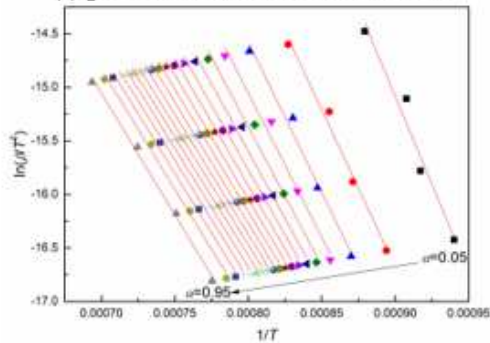
(a) particle size distribution curves



(b) the micro surface morphology



(c) gasification conversion factor curves



(d) the plots of $\ln(\beta/T^2)$ vs $1/T$

Figure 5

Experimental results of five coal samples with different particle sizes: (a) particle size distribution curves; (b) the micro surface morphology; (c) gasification conversion factor curves; (d) the plots of $\ln(\beta/T^2)$ vs $1/T$ at a particular conversion factor

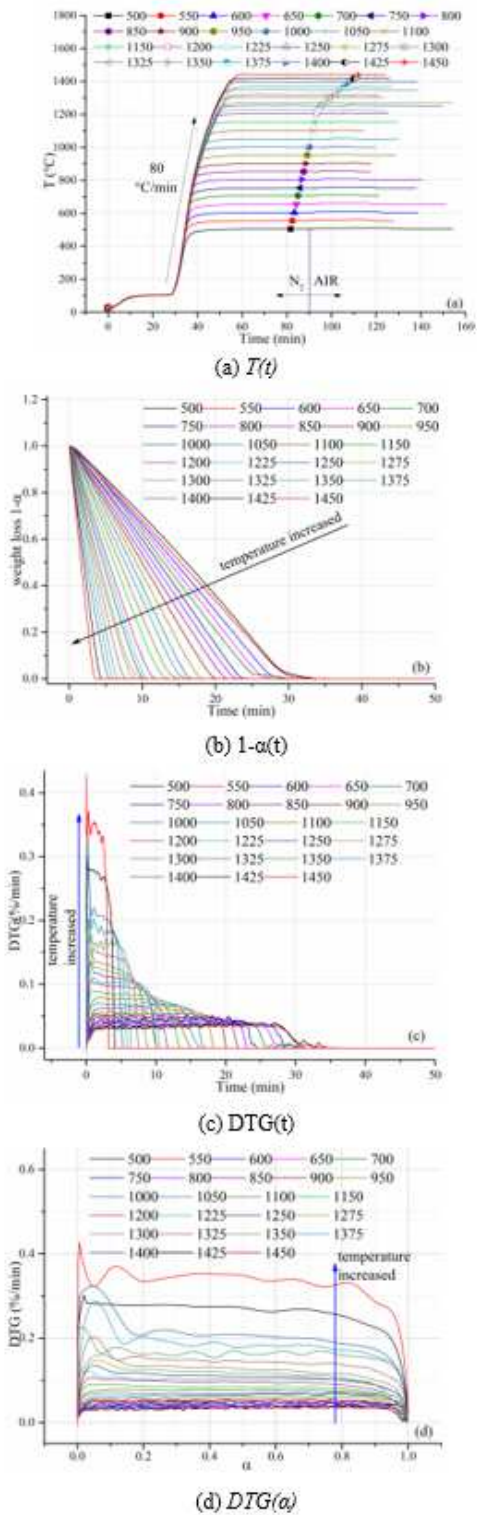
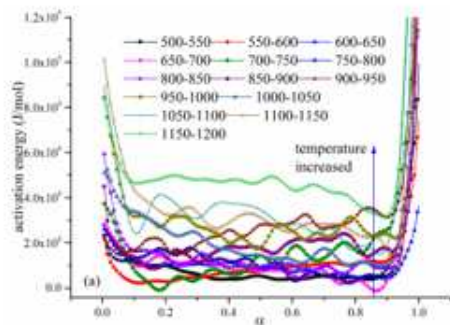
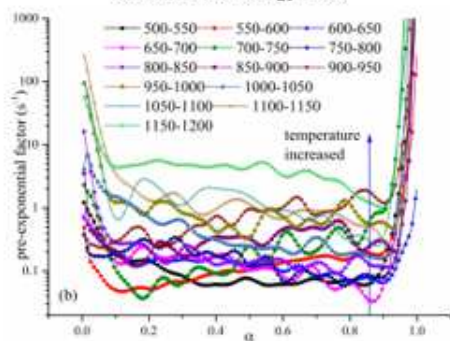


Figure 6

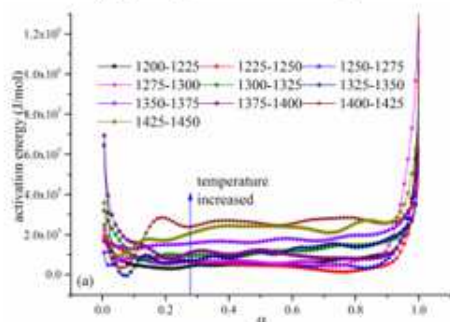
The (a) $T(t)$, (b) $1-\alpha(t)$, (c) $DTG(t)$, and (d) $DTG(\alpha)$ profiles for the Hulunbeier lignite coal.



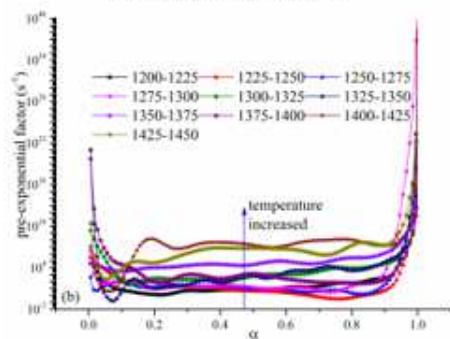
(a) activation energy $E(\alpha)$



(b) pre-exponential factor $A(\alpha)$



(a) activation energy $E(\alpha)$



(b) pre-exponential factor $A(\alpha)$

Figure 7

The results for (a) activation energy $E(\alpha)$ and (b) pre-exponential factor $A(\alpha)$.

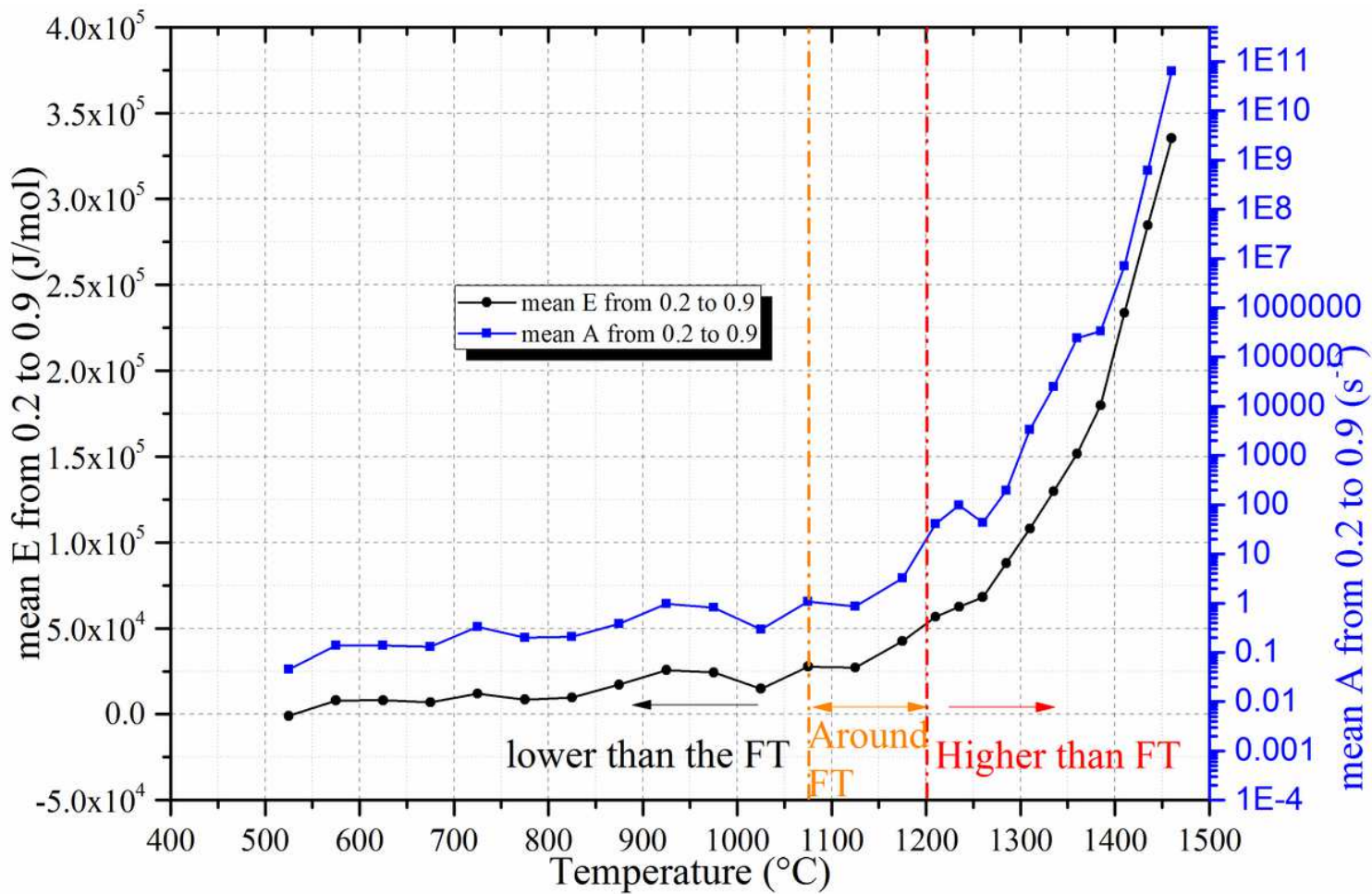
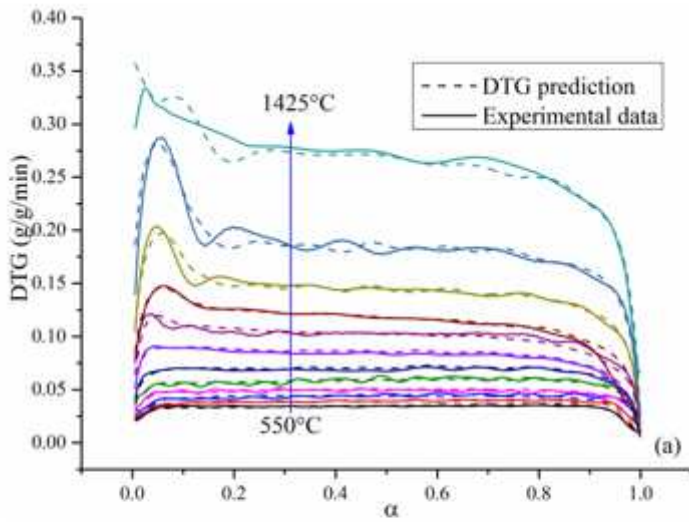
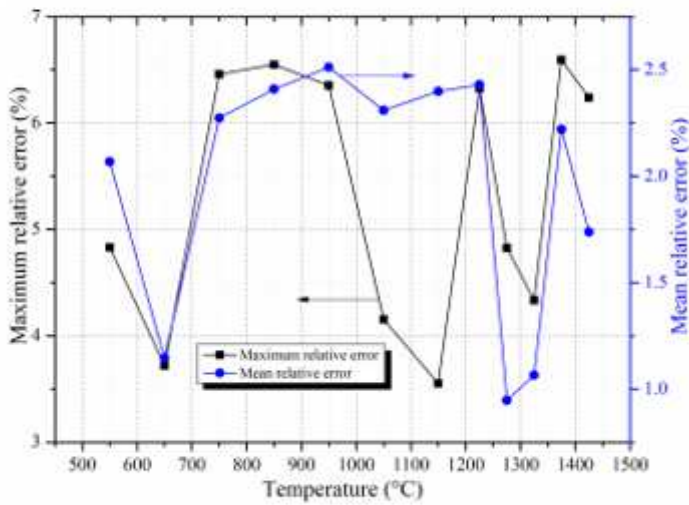


Figure 8

The mean E and A values in the range of $0.2 < \alpha < 0.9$.



(a) predicted results and experimental results



(b) error analysis in the range of $0.2 < \alpha < 0.9$.

Figure 9

Comparison of (a) predicted results and experimental results and (b) error analysis in the range of $0.2 < \alpha < 0.9$

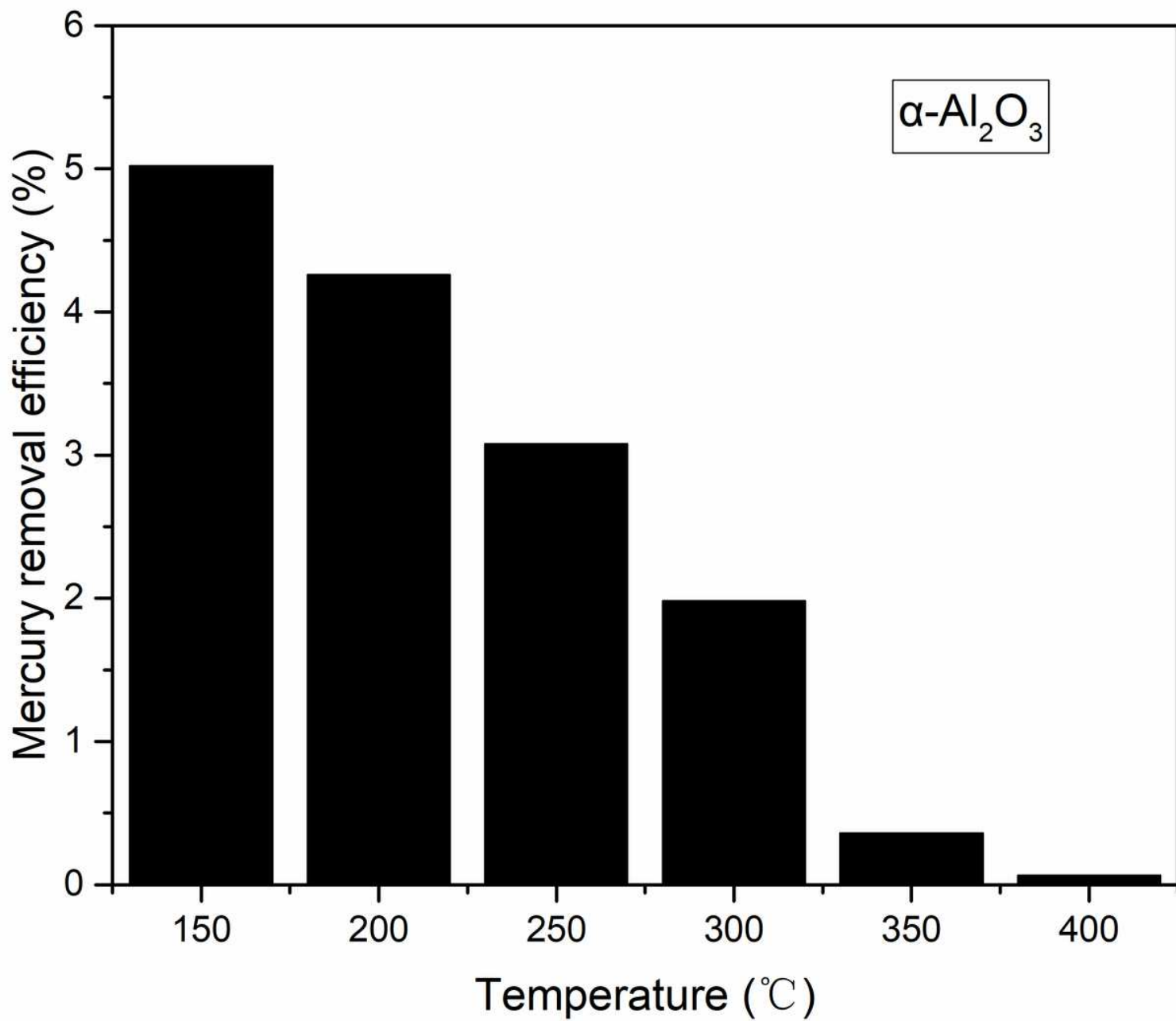


Figure 10

Mercury removal performance of $\alpha\text{-Al}_2\text{O}_3$ at different temperatures

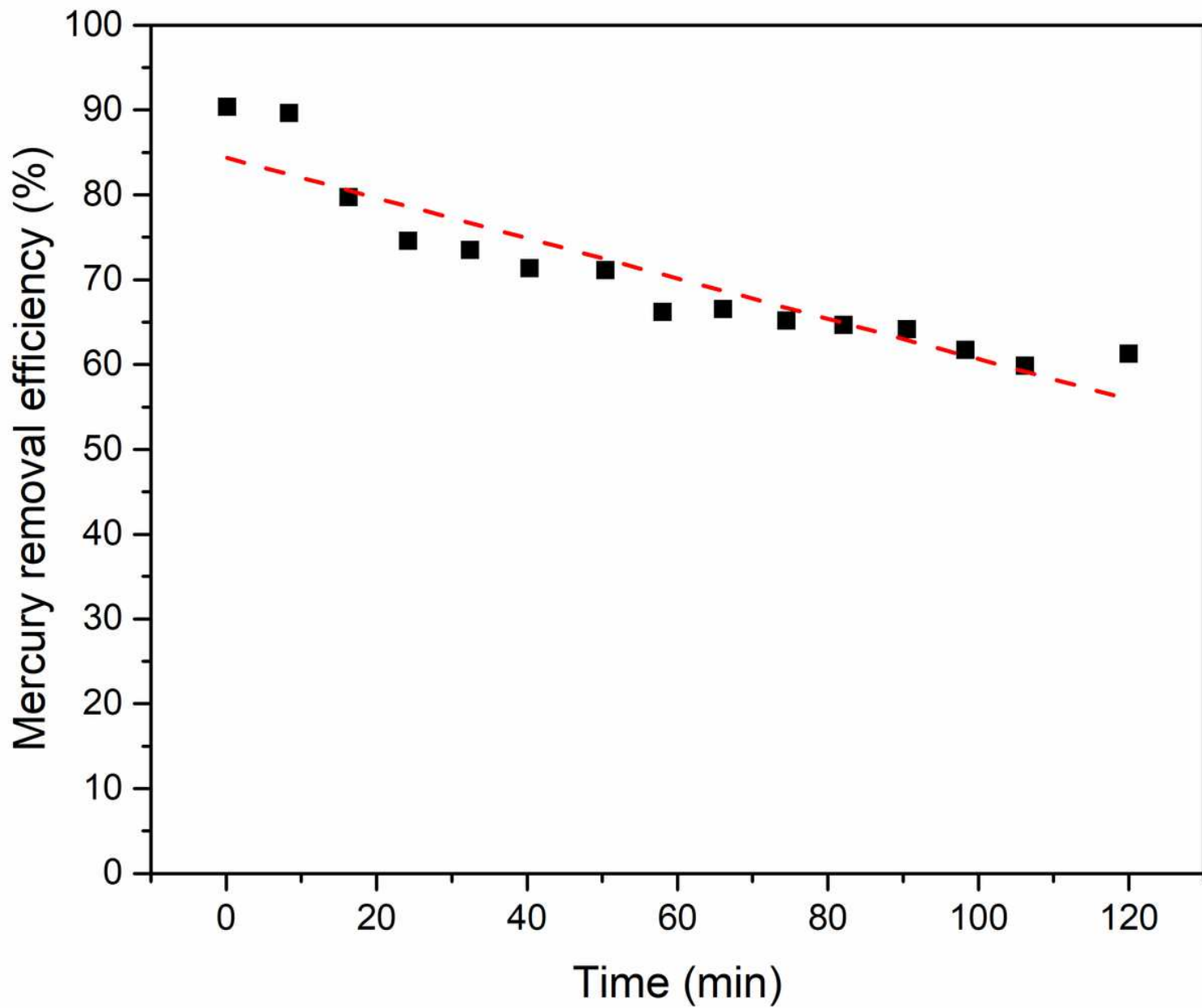


Figure 11

The test curve of mercury removal performance of Mn₂O₃/Al₂O₃

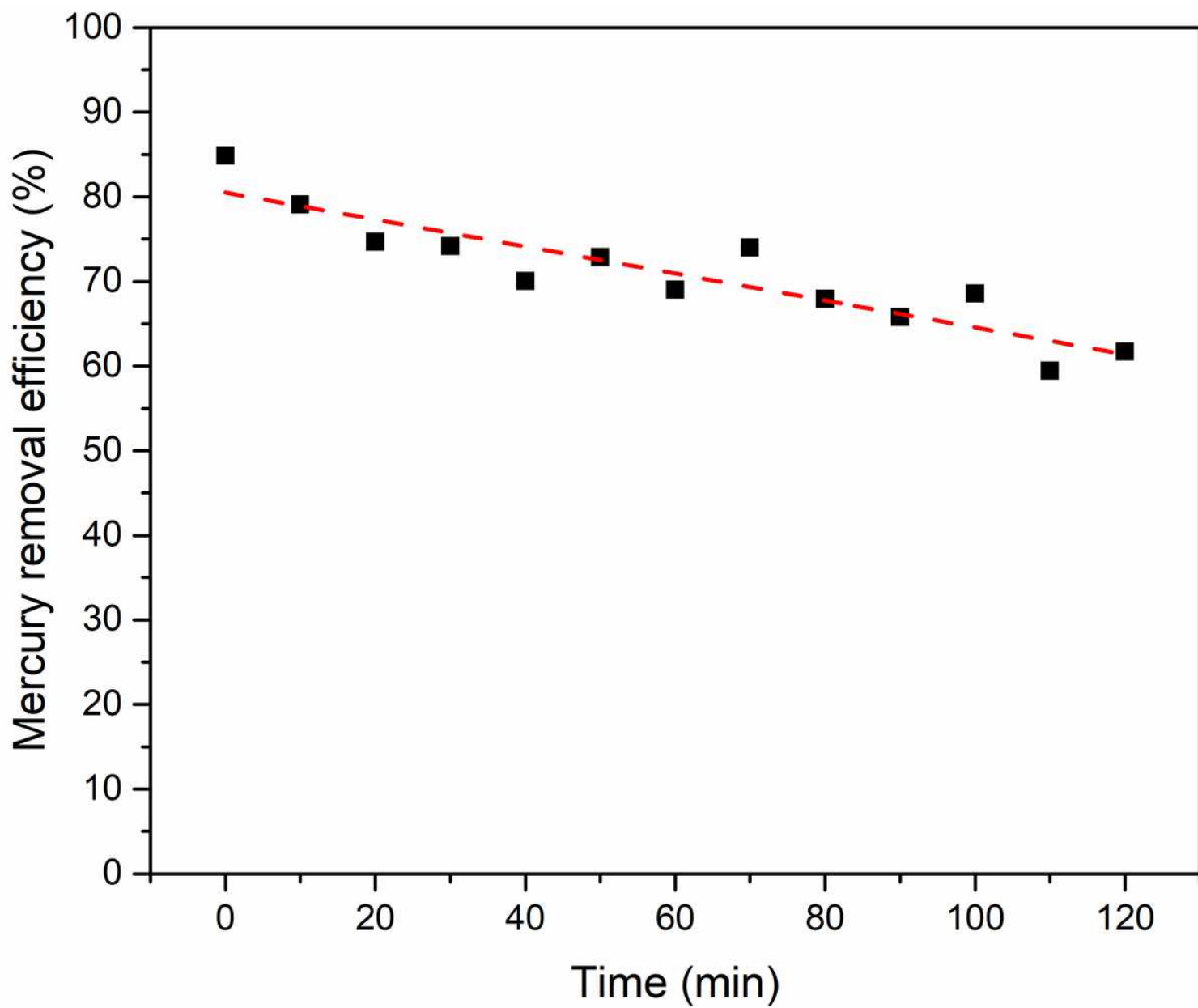


Figure 12

The test curve of mercury removal performance of $\text{Co}_2\text{O}_3/\text{Al}_2\text{O}_3$

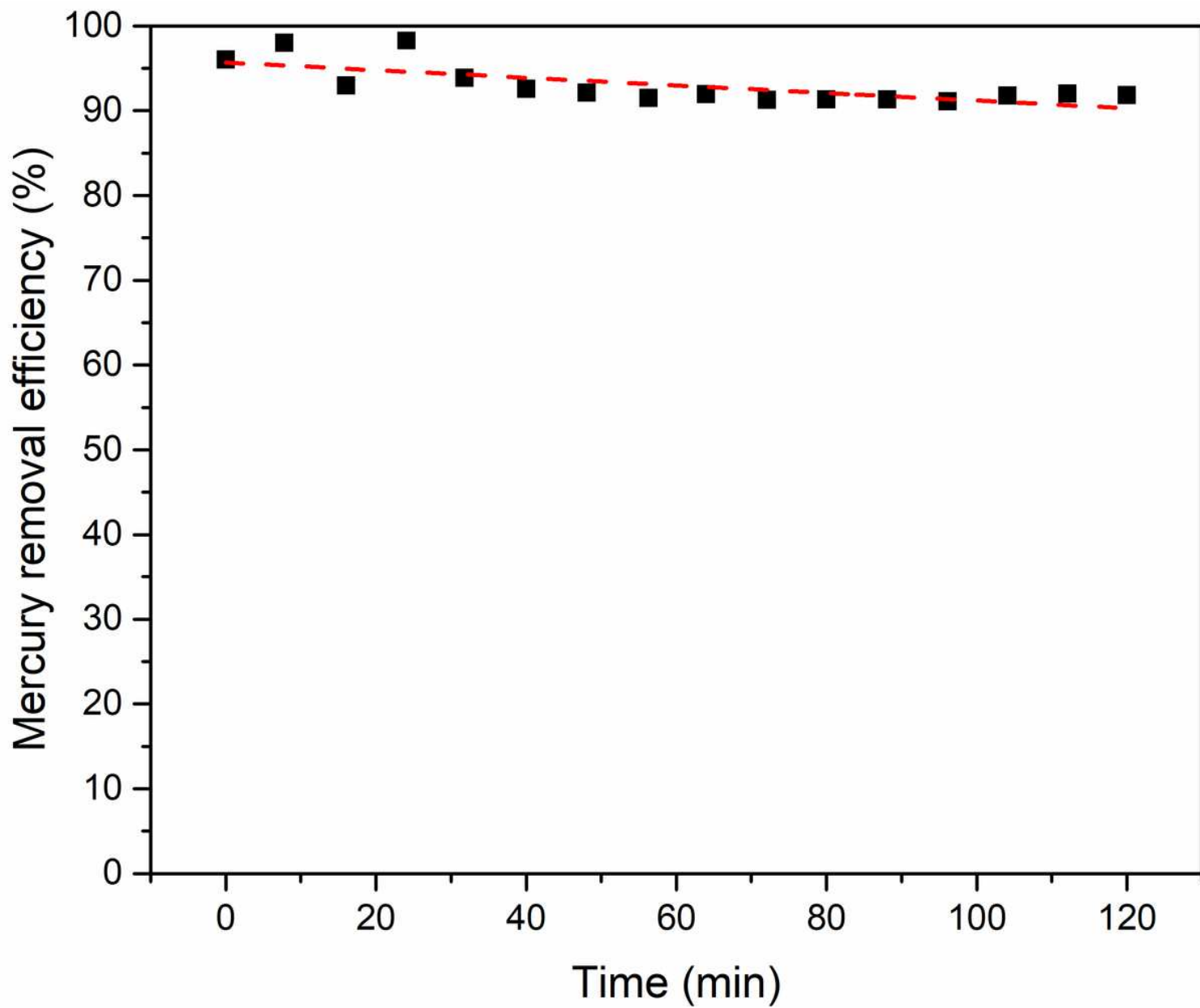


Figure 13

The test curve of mercury removal performance of Fe₂O₃/Al₂O₃